RSC Advances

PAPER

View Article Online
View Journal | View Issue

Cite this: *RSC Adv.*, 2026, **16**, 3325

Enhancing gas sensing and optoelectronic properties of rutile TiO_2 *via* transition metal doping: a DFT + *U* study

Lemma Tirfie Zegbreal,[ab] Newayemedhin Aberra,[a] David E. Motaung,[c] S. Z. Werta[d] and Fekadu Gashaw Hone *[a]

This research employs DFT + *U* calculations to investigate the impact of doping with Co, Ni, Cu, and Zn on the structural, electronic, optical, and gas sensing characteristics of rutile TiO_2. The doping process results in lattice expansion, with optimized lattice constants increasing from 4.630 Å (*a*) and 2.980 Å (*c*) in pure TiO_2 to as much as 4.681 Å and 3.143 Å in Zn-doped systems. This expansion is explained by the variation in atomic radii between Ti and the doped atoms. A reduction in the bandgap is noted across all doped systems (pure: 3.04 eV; Co: 2.51 eV; Cu: 2.63 eV; Ni: 2.66 eV; Zn: 2.56 eV), which enhances the absorption of visible light and promotes p-type conductivity. The analysis of the PDOS indicates significant hybridization among the Ti-3d, O-2p, and dopant 3d orbitals, as well as magnetic properties in the Co, Ni, and Cu-doped systems. The optical properties, including the dielectric function and absorption spectra, further indicate a redshift in all transition metal (TM) doped systems. The gas sensing evaluation shows enhanced detection of CO and NO, with Zn-doping achieving superior selectivity for CO with an adsorption energy of −0.949 eV, while Ni-doping demonstrates a strong affinity for both CO (−0.726 eV) and NO (−0.639 eV), making it suitable for multi-gas detection. Doped rutile TiO_2 systems exhibit enhanced sensitivity, stability, and reusability, positioning them as promising candidates for optoelectronic and gas sensing applications.

Received 17th November 2025
Accepted 4th January 2026

DOI: 10.1039/d5ra08889e

rsc.li/rsc-advances

1. Introduction

The increasing global crisis of air pollution, primarily caused by emissions from industrial and urban sources, has heightened the need for efficient, selective, and cost-effective gas sensors capable of identifying dangerous pollutants such as carbon monoxide (CO) and nitric oxide (NO).[1–3] Among the various semiconductor metal oxides, rutile TiO_2 stands out as a potential chemiresistive sensing material owing to its remarkable chemical stability, non-toxic nature, adjustable surface chemistry, affordability, widespread availability, high-temperature resilience, and ability to withstand harsh environmental conditions.[4] Nevertheless, its practical use is significantly restricted by a large band gap (~3.0 eV), which constrains the generation of charge carriers, as well as by its limited intrinsic selectivity and low response/recovery kinetics.[5]

Doping with transition metals (TMs) is a well-established approach to modify the electronic structure of rutile TiO_2.[6,7] Groundbreaking theoretical research conducted by Saini *et al.* indicated that 3d TM dopants (ranging from Sc to Zn) generate impurity states, which narrow the band gap and may lead to p-type conductivity, particularly with Co, Ni, and Cu.[8] Nevertheless, studies that depend on standard DFT utilizing GGA functionals are inadequate in accurately representing the strongly correlated 3d electrons, resulting in an inaccurate representation of electronic structures.[9] To obtain a physically precise depiction of localized d-states and electronic properties in TMOs, the DFT + *U* method is crucial for correcting the self-interaction error that is characteristic of traditional DFT.[10,11] Samat *et al.* significantly illustrated the importance of this approach for TiO_2, demonstrating that DFT + *U* produces optical properties that are more consistent with experimental findings.[12] Recent studies indicate an increasing focus on correlating these essential electronic alterations with effective gas sensing capabilities. For example, Z. Yan *et al.* integrated experimental methods with DFT to demonstrate that Co-doping improves the NO_2 sensing characteristics of TiO_2 nanotubes, thereby establishing a direct link between a particular dopant and enhanced sensor performance.[13] Similarly, Abd-Elkader *et al.* performed a DFT analysis of TiO_2 quantum dots for different gases, evaluating recovery times to determine

[a]*Department of Physics, Addis Ababa University, P. O. Box: 1176, Addis Ababa, Ethiopia. E-mail: fekadu.gashaw@aau.edu.et*

[b]*Department of Physics, Kotebe University of Education, P. O. Box: 31248, Addis Ababa, Ethiopia*

[c]*Department of Physics, University of the Free State, P. O. Box 339, Bloemfontein ZA9300, South Africa*

[d]*Department of Physics, Dire Dawa University, P. O. Box 1362, Dire Dawa, Ethiopia*

reusability, which is a vital aspect of practical sensor development.[14] Research is often confined to individual dopants or low-dimensional materials, and theoretical analyses frequently employ insufficient functionals or concentrate on a limited range of properties. As a result, a considerable knowledge gap persists: there is currently no systematic and unified computational investigation that thoroughly compares the series of essential transition metal dopants (Co, Ni, Cu, and Zn) within a consistent rutile TiO_2 framework utilizing a robust DFT + U methodology. To address this gap, the present study adopts a robust DFT + U methodology utilizing the Quantum ESPRESSO package to conduct a unified and predictive analysis of Co-, Ni-, Cu-, and Zn-doped rutile TiO_2. By transcending the limitations of previous fragmented studies, it systematically correlates the electronic structure, including band-gap modulation and density of states, with the resultant optical property and gas-sensing behavior towards CO and NO. The sensing potential is quantitatively assessed through adsorption energy, structural stability, recovery time, and reusability across varying temperatures. This integrated framework establishes clear structure property relationships and provides a predictive design principle for the development of high-performance transition metal doped rutile TiO_2 materials for optoelectronic and chemiresistive gas-sensing applications.

2. Computational details

The results found in this paper are investigated on transition metal-doped rutile TiO_2 is studied with supercell approach using the Quantum Espresso package code on the density functional theory (DFT). First, the unit cell of rutile-TiO_2 contains two Ti atoms and four oxygen atoms along with the cell parameters $a = b = 4.599$ Å, $c = 2.959$ Å, $\alpha = \beta = \gamma = 90°$ tetragonal structure used. The rutile TiO_2 crystal with $2 \times 2 \times 2$ supercell model is taken into consideration for the study of the pure TiO_2 and transition metal doping effect. The obtained results and calculations are simulated under the plane wave ultra-soft and norm-conserving pseudopotentials.[15] Our pseudopotentials for the pure and dopants has Ti, O, Co, Ni, Cu and Zn are $3d^2\ 4s^2$, $2s^2\ 2p^4$, $3d^8\ 4s^1$, $3d^9\ 4s^1$, $3d^{10}\ 4s^1$ and $3d^{10}\ 4s^2$, respectively were considered. The exchange–correlation functional is treated using generalized gradient approximation (GGA) of Perdew–Burke–Ernzerhof (PBE).[16] For kinetic energy cutoff, 80 Ry, which has been obtained from the convergence calculation seen in Fig. S1(a), and for charge density cutoff 640 Ry were used throughout the study. The special points sampling integration in the Brillouin zone were employed using the Monkhorst–Pack method with $6 \times 6 \times 5$ special k-points mesh in all self-consistent field calculations, which was obtained from the convergence calculations shown in Fig. S1(b), has been used. In our simulations, the total energy and force convergence was set at 10^{-6} eV and 10^{-3} eV Å^{-1}, respectively. For band structure calculations the high symmetry k-point was used for the convenient purpose. To achieve high-resolution dispersion curves, the path was sampled along the Γ–X–M–Γ–Z–R–A path, utilizing a density of 20 k-points per segment to accurately capture the electronic transitions. For total and projected density of states calculations, the high dense k-points $18 \times 18 \times 15$ was used in order to investigate more around the Brillion zone. The standard GGA underestimates the energy bandgap of transition metal oxides.[17,18] Due to this limitation, the Hubbard correction (U), which introduces a correction for the self-interaction of the Ti localized d orbital, is used. In this study, on-site Hubbard corrections were implemented within the DFT + U framework to accurately capture the localized characteristics of transition-metal 3d electrons. The U values were determined based on well-established literature benchmarks instead of being fitted to specific systems. For Ti-3d states, a U value of 7.5 eV was utilized, which is commonly cited as effectively reproducing the experimental band gap and electronic structure of rutile TiO_2.[15,19] For the dopant 3d states, U values of 4.0 eV (Co), 5.0 eV (Ni), 5.0 eV (Cu), and 4.0 eV (Zn) were chosen in line with previous computational investigations of transition-metal-doped TiO_2 and related oxides.[20–24] These values ensure a physically reasonable localization of the dopant 3d electrons and support the experimentally relevant +2 oxidation states of the impurities. All U parameters were kept fixed throughout all calculations to ensure a consistent and transferable theoretical framework for evaluating the impacts of various dopants. The crystal geometry was fully optimized by using relax and variable cell relaxation calculation, and to find the ground state energy, we have used the Broyden Fletcher Goldfarb Shanno (BFGS) minimization method. For crystal structure visualization, modeling, and designing we have used XCrySDen, BURAI and VESTA software.

3. Results and discussions

3.1 Structural optimization

A rutile TiO_2 has a tetragonal crystal structure with a basis in which the two Ti are positioned at (0, 0, 0) and (1/2, 1/2, 1/2), and the four oxygen atoms are at position $\pm(u, u, 0, 1/2 + u, 1/2 - u, 1/2)$ with $u = 0.233$ (ref. 25) and is categorized in a space group of group $p4_2/mnm$ number 136. The unit cell of rutile TiO_2 is characterized by lattice constants $a = b$ and c which were determined to be $a = b = 4.59$ Å, $c = 2.96$ Å, while $\alpha = \beta = \gamma = 90°$, sourced from the materials project as illustrated in Fig. S2(a).[16] Structural optimization results obtained in this work yield that the lattice constants, $a = b$ and c at the minimum energy to be 4.630 Å and 2.980 Å, respectively, as depicted in Fig. 1(a) and (b). These lattice constants were used for creating a $2 \times 2 \times 2$ supercell consisting of 48 atoms of $Ti_{16}O_{32}$ as shown in Fig. S2(b).

Following the structural optimization of pure rutile TiO_2, the structure of transition-metal doped TiO_2 was optimized utilizing the same ultra-soft pseudopotentials, with their lattice parameters detailed in Table 1. These parameters were observed to increase compared to the corresponding values of the pure structure. Notably, the calculated lattice parameters closely align with both experimental and theoretically established values.[16,26,27] This phenomenon is attributed to the substitution of Ti^{4+} (0.605 Å) with transition metals possessing larger ionic radii, such as Co^{2+} (0.745 Å), Ni^{2+} (0.690 Å), Cu^{2+} (0.730 Å), and Zn^{2+} (0.740 Å), which consequently results in an increase in the

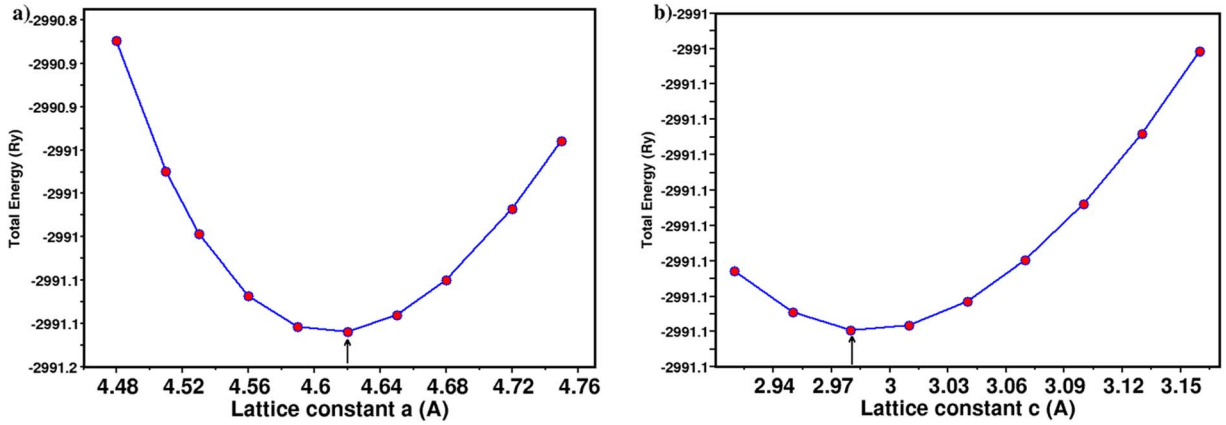

Fig. 1 The graph depicting total energy (Ry) against lattice parameter (Å): (a) lattice constants $a = b$ and (b) lattice constant c.

Table 1 Lattice parameters, bond lengths, and bond angles for the fully optimized geometry of pure rutile TiO_2, as well as doped rutile TiO_2

Materials	Lattice parameters $a = b$	c	V (Å)^3	Bond length (Å)	Bond angle (°)
Pure rutile TiO_2	4.63	2.98	63.88	Ti–O = 2.01 Ti–O = 1.95	O–Ti–O = 90.00
Co-doped TiO_2	4.68	3.09	67.68	Co–O = 2.08 Co–O = 2.00	O–Co–O = 91.20
Cu-doped TiO_2	4.66	3.13	67.97	Cu–O = 2.1 Cu–O = 1.99	O–Cu–O = 92.50
Ni-doped TiO_2	4.67	3.10	67.74	Ni–O = 2.04 Ni–O = 1.98	O–Ni–O = 91.00
Zn-doped TiO_2	4.68	3.14	68.87	Zn–O = 2.09 Zn–O = 2.00	O–Zn–O = 91.40

unit cell volume, as illustrated in Table 1. Furthermore, a structural distortion in the doped TiO_2 was observed, evidenced by the increases in bond lengths and angles, namely α, β, and γ. This led to a localized lattice expansion, resulting in octahedral distortion.[28]

3.2 Electronic structure

3.2.1 Band structures of pure and TM (Co, Cu, Ni and Zn) doped rutile TiO_2. The electronic band structures of both pure and TM-doped rutile TiO_2 were computed to gain insights into their electronic properties, as depicted in Fig. 2(a–f). The computation was performed using high symmetry k-points located within the Brillouin zone. To clarify the concept of crystal momenta in our analyses, the electronic band structure was calculated along a detailed high-symmetry path within the first Brillouin zone of the 2 × 2 × 2 tetragonal supercell: Γ–X–M–Γ–Z–R–A–Z|X–R|M–A. The fractional coordinates of these points in reciprocal space are Γ (0,0,0), X (0.5,0,0), M (0.5,0.5,0), Z (0,0,0.5), R (0.5,0,0.5), and A (0.5,0.5,0.5). These points correspond to the first Brillouin zone of the enlarged supercell, and the labels are clearly depicted in Fig. 2. This ensures that the dispersion curves are distinctly defined and entirely reproducible. Within the Quantum ESPRESSO framework, the Fermi energy (E_F) is calculated self-consistently during the SCF process by ensuring the charge neutrality of the periodic supercell. For the semiconducting systems examined in this study, E_F lies within the band gap. In this case, it is placed between the highest occupied and lowest unoccupied Kohn–Sham states according to the electronic occupation, without corresponding to a single eigenvalue. No manual shifting or post-processing alignments were performed. For consistent visual comparison across all systems, E_F is set to 0 eV in all electronic structure plots (band structures and PDOS).

The band gap of pure rutile TiO_2 was determined to be 1.77 eV through uncorrected GGA calculations, which aligns with theoretical predictions[16] illustrated in Fig. 2(a). However, this value was significantly lower than the experimentally measured value due to the GGA functionals underestimation of Ti 3d states. Hence, a Hubbard U correction (DFT + U) was applied, resulting in a band gap of 3.02 eV for pure rutile TiO_2, as depicted in Fig. 2(b), which is an excellent agreement with the experimentally determined value.[19] Additionally, the electronic structure of rutile TiO_2 calculated using DFT + U indicated that the CBM and the VBM are located at the same k-point (Γ point), thereby confirming its direct band gap semiconductor property, while its the Fermi level was observed to be nearer to the VBM, further indicating that the material is a p-type semiconductor.[18]

The electronic structure of the TM-doped materials illustrated in Fig. 2(c–f) also demonstrated that the direct band gap characteristic is maintained. These band structures correspond to a 6.25% doping concentration, modeled by a single substitution in a 2 × 2 × 2 supercell. The apparent dispersion of the dopant-induced states (spaghetti-like bands) arises from the artificial periodicity of the supercell. In practical scenarios involving disordered doping, these impurity levels would be essentially k-independent, appearing as flat bands or discrete energy levels. Nevertheless, the supercell approach provides a consistent theoretical baseline for analyzing the electronic transitions introduced by the dopant at this concentration.[8]

The CBM (VBM) for Co, Cu, Ni, and Zn-doped TiO_2 were determined to be 2.53 (0.02) eV, 2.89 (0.26) eV, 2.05 (−0.61) eV,

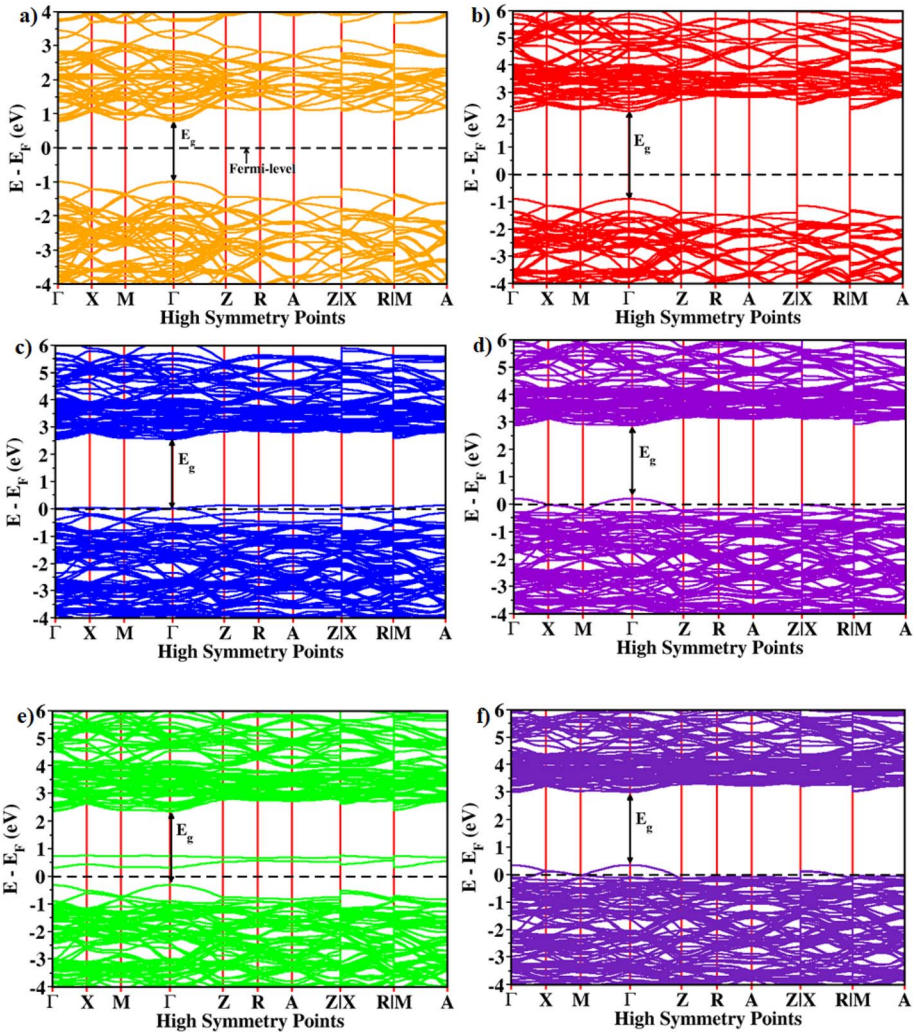

Fig. 2 Electronic band structures for (a) GGA pure rutile TiO_2, (b) GGA + *U* pure rutile TiO_2, (c) GGA + *U* Co-doped rutile TiO_2, (d) GGA + *U* Cu-doped rutile TiO_2, (e) GGA + *U* Ni-doped rutile TiO_2, and (f) GGA + *U* Zn-doped rutile TiO_2.

and 2.94 (0.38) eV, respectively, with corresponding band gaps of 2.51 eV, 2.63 eV, 2.66 eV, and 2.56 eV respectively. It is clear that the band gap of pure rutile TiO_2 can be significantly reduced through doping, which is expected to enhance the electrical conductivity of the doped materials, thereby improving their gas-sensing capabilities. The observed decrease in bandgap can be attributed to the expansion of the unit cell when the larger atomic radii TM substitute Ti^{4+} as discussed above. It was noted that the Fermi level of the doped samples is lowered towards the VBs and resides within defect-induced valence states, thereby confirming their p-type semiconducting nature. Moreover, the observed bandgap reduction and the type of conductivity across all dopants underscores a promising strategy to push the absorbance of the pure TiO_2 to the visible, enabling enhanced performance in visible-light-driven applications such as optoelectronics and gas sensing, as supported by both experimental and theoretical findings.[8,19,29,30]

3.2.2 Total and partial density of state of pure and doped rutile TiO_2. In this section, we analyze the partial density of states (PDOS) and total density of states (TDOS) for both pure rutile TiO_2 and rutile TiO_2 doped with Co, Cu, Ni, and Zn, as shown in Fig. 5, to investigate the orbital interactions of each atom. The valence band in pure rutile TiO_2 is predominantly composed of O 2p orbitals, while the conduction band is mainly formed by Ti 3d orbitals, indicating a significant ionic bonding between Ti and O, as demonstrated in Fig. 3(a). The band gap of pure TiO_2 was determined to be 3.04 eV, which further confirm the results obtained using DFT + *U* in the preceding section. Moreover, the spin-up and spin-down states were observed to be symmetrical (refer to Fig. 3(a)), indicating its non-magnetic nature.

Following doping, the Fermi level of the TM-doped TiO_2 shifted further into the VB accompanied by the dopant-derived states near the band edges, which effectively narrowed the bandgap to a range of 2.66–2.51 eV, as illustrated in Fig. 3(c)–(e), while maintaining the p-type conductivity of the pure TiO_2. This modification will enhance the absorption of visible light. Moreover, in the case of the introduction of dopants similar to pure rutile TiO_2, the VB is predominantly formed from

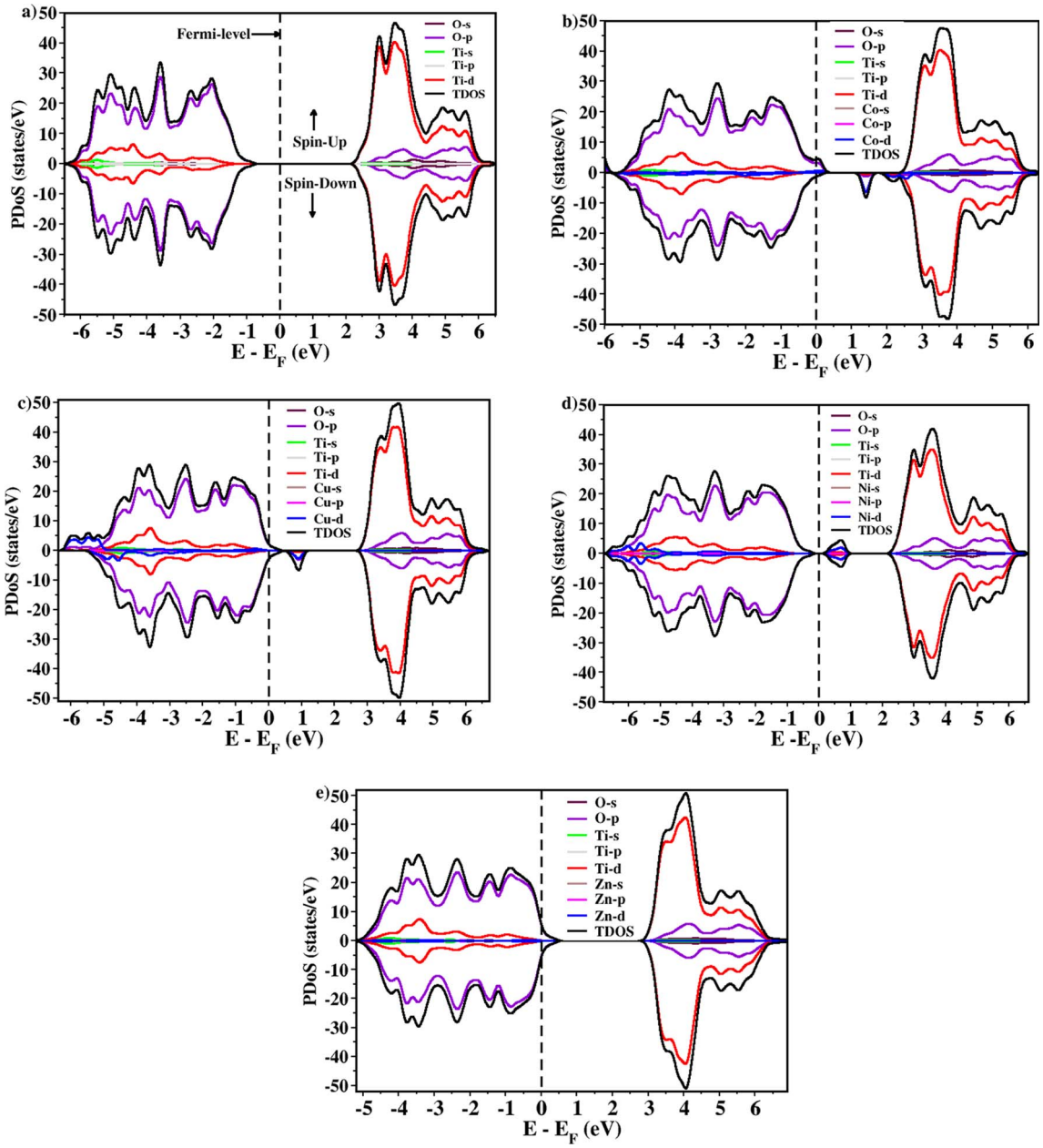

Fig. 3 The total and partial density of states GGA + *U* for (a) pure rutile TiO_2, (b) Co-doped rutile TiO_2, (c) Cu-doped rutile TiO_2, (d) Ni-doped rutile TiO_2, and (e) Zn-doped rutile TiO_2.

contributions of the O 2p orbitals, while the CB is primarily influenced by the Ti 3d orbitals, nevertheless, the 3d orbitals of the dopants introduce supplementary states near the band edges, which significantly alter the electronic and magnetic characteristics.

Among the four dopants, Co, Ni, and Cu-doped TiO_2 demonstrate spin asymmetry in the PDOS, indicating the introduction of magnetic behavior, whereas Zn-doped TiO_2 maintains spin symmetry and is non-magnetic. The magnetic property that was introduced by the three dopant is due to their unpaired d electron that is responsible for creating local magnetic moment as can be seen in their electronic configurations as Co^{2+} ($3d^7$), Ni^{2+} ($3d^8$), and Cu^{2+} ($3d^9$) while the full d orbital in Zn^{2+} ($3d^{10}$) led to spin pairing that will cancel out the magnetic moment in the Zn doped rutile TiO_2. The effective +2 oxidation state of the transition-metal dopants was determined by Bader charge analysis, which quantified net charge transfer consistent with divalent cations, and is further supported by the calculated local magnetic moments matching the expected high-spin TM^{2+} configurations.[31,32] Charge compensation during the aliovalent substitution of Ti^{4+} by TM^{2+} is achieved through the generation of holes in the valence band, leading to a downward shift of the Fermi level into the valence states and confirming the observed p-type semiconducting behavior upon doping.[33,34] From a chemical perspective, the incorporation of transition-metal dopants generates localized TM-3d states that

engage with lattice O-2p orbitals. This hybridization alters the density of states close to the band edges, resulting in available electronic states that improve the surface's chemical reactivity, thereby establishing a basis for effective adsorption and redox processes.

The results of the PDOS analysis indicate that Co 3d states are located close to the CBM, thereby introducing shallow donor levels. In contrast, Ni and Cu 3d states are predominantly found near the VBM, creating acceptor-like states that improve hole conductivity. Conversely, Zn 3d orbitals are situated deep within the valence band, contributing minimally to the states near the Fermi level. These differences illustrate the gradual filling of the 3d orbitals from Co to Zn, which influences both the hybridization strength with Ti 3d and O 2p orbitals and the positioning of states induced by dopants. In particular, for the Ni-doped system, the PDOS indicates robust hybridization between Ni-3d states and lattice O-2p orbitals, leading to an elevated density of electronic states near the Fermi level. This electronic characteristic offers accessible pathways for bidirectional charge transfer with adsorbed molecules and signifies a crucial chemical aspect underlying the dual affinity of Ni-doped TiO_2 for both CO and NO gases. In summary, in addition to the electronic and magnetic alterations, the PDOS exhibits characteristics that are significantly useful to gas sensing such as (i) the presence of dopant-induced shallow states near to the Fermi level facilitates enhanced charge transfer between the surface and the adsorbed gas molecules, thereby increasing sensitivity, (ii) magnetic dopants such as Co, Ni, and Cu create active sites that interact with paramagnetic gases like NO, which in turn influences the energetics of adsorption and the behavior of the response, and (iii) an elevated PDOS near the band edges leads to an increase in carrier density beneficial for gas sensing through reduction/oxidation.

3.3 Optical properties

In this section, we examine the optical characteristics of pure rutile TiO_2 and the impact of TM doping at a fixed concentration of 6.25% (one Ti atom replaced per $2 \times 2 \times 2$ supercell containing 16 Ti sites). To explore these optical properties, we have computed the dielectric function, which consists of three components: $\varepsilon_{xx}(E)$, $\varepsilon_{yy}(E)$, and $\varepsilon_{zz}(E)$. For all optical calculations, we averaged these three components. Given that our calculations incorporate spin-polarized data, we combined the spectra for both spin-up and spin-down states for pure and TM-doped rutile TiO_2, resulting in a single optical plot for each system.[35]

The available optical transition states in both pure and TM-doped TiO_2 were determined by analyzing their joint density of states (JDOS) across an energy spectrum of 0–15 eV, as illustrated in Fig. 4. This is mathematically represented as $\hbar\omega = \sum\_(k,n,m)\delta(E_m, k - E_n, k - \hbar\omega) \times f(E_n, k) \times [1 - f(E_m, k)]$, where $\hbar\omega$ is photon energy, E_n, k represents the nth energy band at the k-point K, while $f(E)$ and δ are Fermi-Dirac and Dirac delta functions, respectively. The JDOS curves calculated for the materials under investigation indicate an increase in transition states with doping, ranked in the following order: Co > Cu > Zn > Ni in comparison to the pristine state. These optical properties are specific to the studied doping concentration and may vary with different dopant densities.

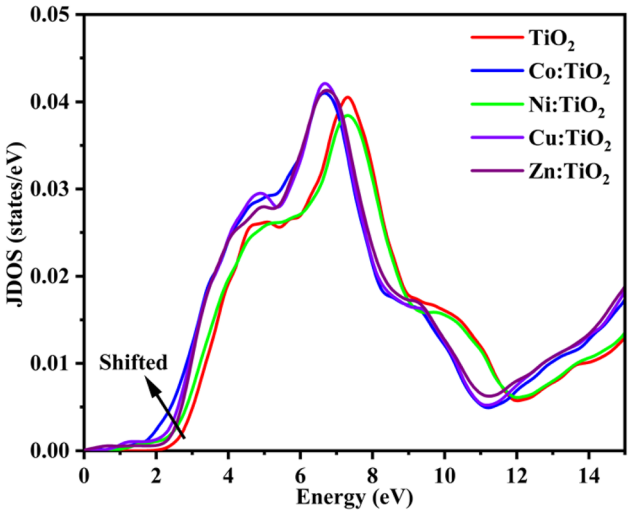

Fig. 4 Joint density of states (JDOS) *versus* photon energy for pure rutile TiO_2 and for rutile TiO_2 doped with Co, Ni, Cu, or Zn at a concentration of 6.25%.

The optical properties, namely refractive index, absorption and reflectivity, of the materials at the studied doping concentration are further determined after calculating their real (ε_1) and imaginary dielectric (ε_2) spectra's given in Fig. S3(a) and (b). The spectra distinctly demonstrate that dopants significantly influence the polarizability at this concentration, suggesting their additional role in the gas sensing mechanism when incorporated into gas sensors. It is crucial to note that the optical properties presented in this study pertain specifically to the modeled doping concentration of 6.25%. Although qualitative trends across various dopants may remain consistent, the quantitative metrics, including the refractive index and dielectric constant, are anticipated to fluctuate with variations in dopant density. This fluctuation is attributed to alterations in the collective electron response and the onset of dopant–dopant interactions. The real (n) and imaginary (k) parts of the refractive index ($\bar{n}(\omega) = n(\omega) + ik(\omega)$) for the studied materials were derived using eqn (1) and (2);[19,36]

$$n(\omega) = \sqrt{\frac{\sqrt{\varepsilon 1^2(\omega) + \varepsilon 2^2(\omega)} + \varepsilon 1(\omega)}{2}}, \quad (1)$$

and

$$k(\omega) = \sqrt{\frac{\sqrt{\varepsilon 1^2(\omega) + \varepsilon 2^2(\omega)} - \varepsilon 1(\omega)}{2}} \quad (2)$$

The refractive index spectra of the materials show a high refractive index within the visible spectrum, as illustrated in Fig. 5(a). Additionally, it is observed that doping at 6.25% has a negligible effect on the refractive index spectra, particularly in the energy range below 4 eV, with the exception of Zn-doped

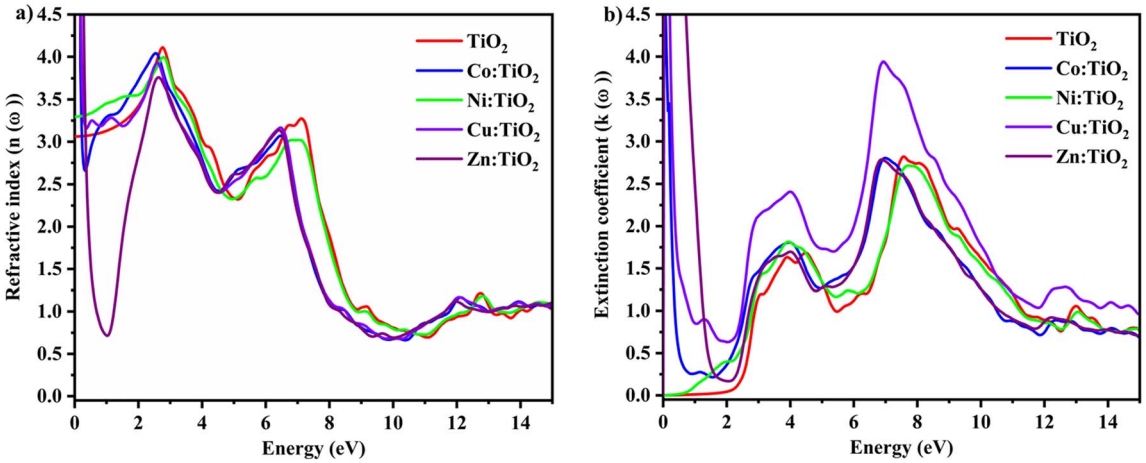

Fig. 5 (a) Refractive index and (b) extinction coefficient as a function of photon energy for pure and 6.25% TM-doped rutile TiO_2.

TiO_2, which is attributed to its lower real dielectric function in that region. Moreover, the extinction coefficient spectra demonstrate that Cu-doped TiO_2 exhibits the highest extinction at low energy levels, whereas Ni-doped TiO_2 presents the lowest values at this specific doping level. In contrast, the pure material shows an onset around 3 eV, thereby confirming the effective influence of the dopants in our model on the shifting of their band gap, as depicted in Fig. 5(b).

Following to this, the absorption coefficient spectra were computed utilizing eqn (3):

$$\alpha(\omega) = \frac{4\pi k(\omega)}{\lambda},\ \lambda = hc/E \tag{3}$$

The results further confirmed that with doping at the modeled concentration, a red-shift of the absorption onset of TiO_2, originally at 3 eV, thereby reducing the band gap of the studied TM-doped systems as illustrated in Fig. 6(a). This reduction in the band gap enhances the efficiency of electron injection and withdrawal in the gas sensing mechanism when employing this material, as the majority of gases possess oxidation/reduction energy levels within this region. Finally, the reflectivity spectra of the materials are determined using eqn (4).

$$R(\omega) = \frac{(n(\omega)-1)^2 + k(\omega)^2}{(n(\omega)+1)^2 + k(\omega)^2} \tag{4}$$

In the visible region, all the materials have highest reflectivity below 2 eV consistent with their much lower absorption coefficients in the region. Furthermore, as illustrated in Fig. 6(b), both Ni-doped and pure TiO_2 demonstrate the lowest reflectivity under 2 eV. Evidently, higher energy photons are reflected by the pure and studied TM-doped TiO_2 which confirms their excellent UV-screen property.

3.3.1 Optical conductivity ($\sigma(\omega)$). The optical conductivity of the materials at the studied doping concentration was calculated using eqn (5), aiming to understand the dynamics of charge carriers induced by photons, which arise from interband transitions within the energy spectrum of 0–15 eV, as illustrated in Fig. 7.

$$\sigma(\omega) = \frac{\varepsilon 2(\omega)\alpha(\omega)}{4\pi} \tag{5}$$

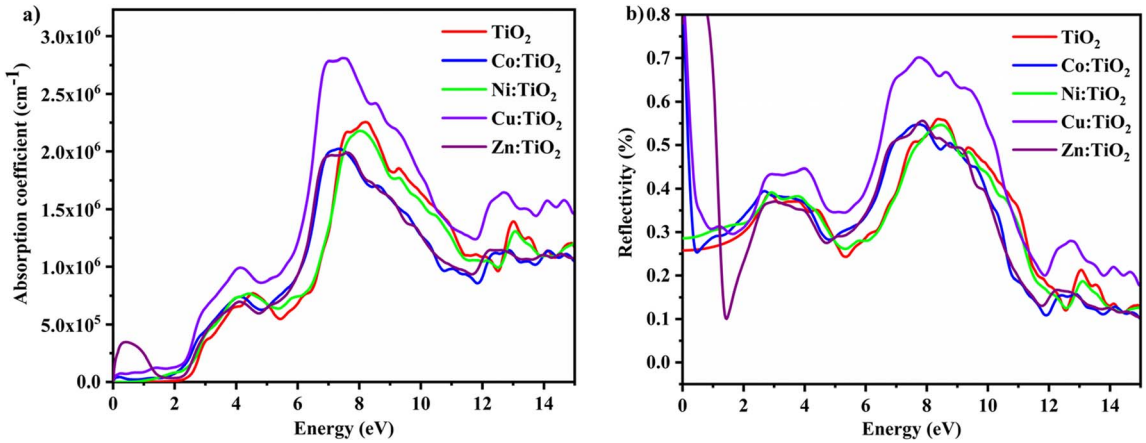

Fig. 6 (a) The absorption coefficient (α (cm^{-1})), (b) the reflectivity as a function of photon energy for pure and 6.25% TM-doped rutile TiO_2.

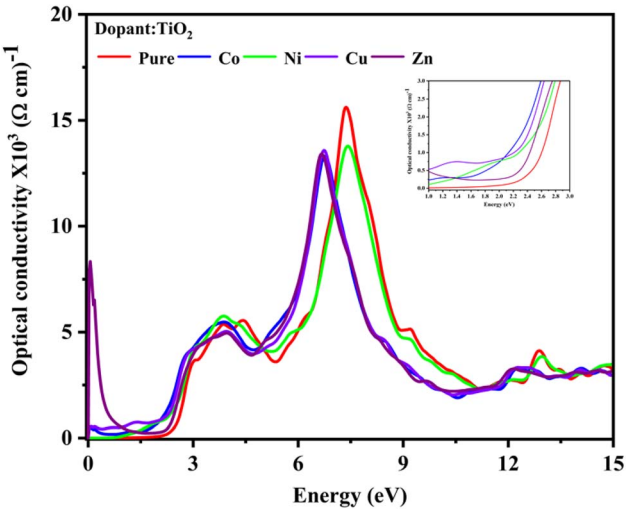

Fig. 7 The optical conductivity against photon energy of pure and 6.25% TM-doped rutile TiO_2.

The optical conductivity spectra of pure TiO_2 reveal two prominent peaks, with the most pronounced peak occurring at approximately 8 eV, indicating substantial interband transitions from the O 2p valence band to the Ti 3d conduction band. At a concentration of 6.25%, the introduction of Co, Ni, Cu, and Zn dopants modifies the optical conductivity, especially in the visible region, and results in a reduction of the bandgap compared to pure rutile TiO_2. This reduction enhances optical conductivity at lower energy levels. A recognized limitation for gas sensing under visible light is that the relatively low conductivity of TiO_2 below 3 eV suggests limited photon-induced carrier generation in the visible spectrum, despite this confirming the material's significant optical activity in the UV region.[40] This increased conductivity observed in the doped materials at this concentration may be attributed to the presence of structural defects. Generally, all studied systems exhibit a decline in optical conductivity as the photon energy rises. Recent experimental and theoretical investigations support these findings, which also validate the trends observed in other optical parameters such as extinction and absorption coefficients.

3.4 Gas sensing analysis

To elucidate the essential sensing mechanisms, this section presents a comprehensive analysis of gas sensing capabilities of pure and TM-doped rutile TiO_2 for the detection of CO and NO (see Fig. 8). Special emphasis is placed on adsorption energy, stability, recovery dynamics, reusability, and sensing mechanisms. To simulate the gas-sensing interface, periodic slab models of the rutile TiO_2 (110) surface were employed, representing the most thermodynamically stable and experimentally relevant facet for gas–surface interactions.[37–40] The models were constructed as a 2×2 supercell with cell parameters of 9.26 Å × 9.26 Å in the *xy*-plane and 25.96 Å along the *z*-direction. This configuration corresponds to a slab thickness of approximately 5.96 Å (containing 4 atomic layers of TiO_2) with a vacuum region of 20.0 Å along the surface normal to eliminate spurious interactions between periodic images.[41]

The surface was modeled with the stoichiometric, oxygen-bridged termination that exposes characteristic rows of five-fold coordinated titanium (Ti_{5C}) atoms and two-fold

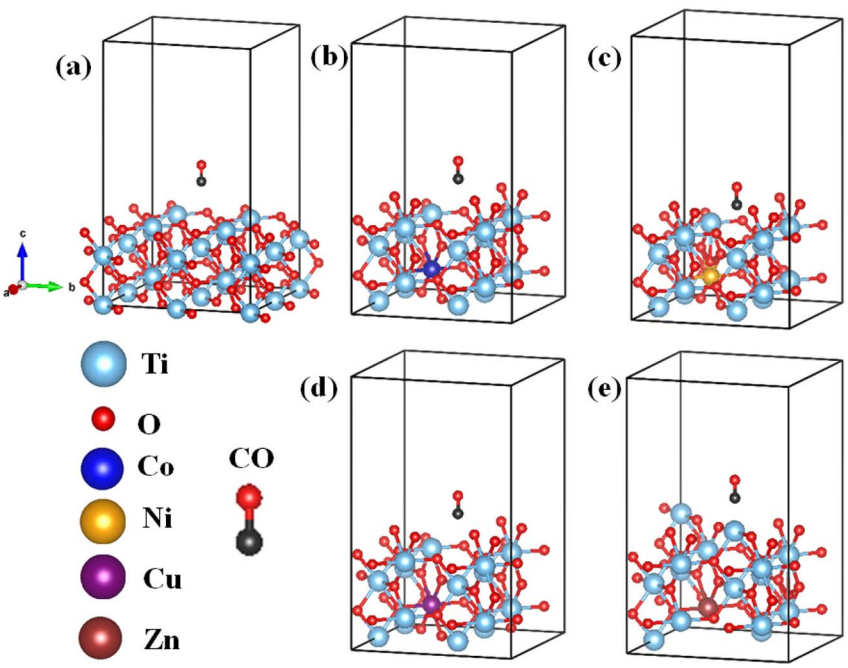

Fig. 8 The arrangement of the CO gas molecule on the surface of pure rutile TiO_2 and various doped rutile TiO_2 types is depicted as follows: (a) CO on rutile TiO_2, (b) CO on Co-doped TiO_2, (c) CO on Ni-doped TiO_2, (d) CO on Cu-doped TiO_2, and (e) CO on Zn-doped TiO_2. For the NO gas molecule, we have employed a similar configuration over the surfaces of pure and doped rutile TiO_2 as illustrated in this figure.

coordinated bridging oxygen atoms. This termination represents the standard rutile TiO_2 (110) surface that has been extensively characterized in both experimental and theoretical studies.[37] During structural optimization, all atoms in the system (surface, dopant, and adsorbates) were allowed to relax fully without constraints, with the in-plane lattice parameters fixed to the optimized bulk values. The choice of full relaxation was made to accurately capture the structural reorganization induced by doping and gas adsorption, particularly important for transition metal dopants that may induce significant local distortions.

The adsorption of CO and NO was systematically investigated by exploring multiple adsorption configurations at the exposed Ti_{5C} sites, which have been established as the primary active centers for gas interaction on TiO_2 (110).[42] For each Ti_{5C} site, we tested: (i) atop adsorption with the molecule perpendicular to the surface (CO: C-down and O-down; NO: N-down and O-down); (ii) tilted configurations with angles ranging from 90° to 180° relative to the surface normal; and (iii) bridge configurations between Ti_{5C} and neighboring oxygen sites. We have examined various sites to identify distinct initial geometries per gas molecule per doped system were optimized to ensure convergence to the global minimum energy configuration. This systematic approach ensured comprehensive sampling of the conformational space while maintaining consistency with established adsorption geometries reported in the literature.[14]

3.4.1 Adsorption energy and stability. The strength of interaction between gas molecules and sensing materials is greatly affected by the adsorption energy (E_{ads}). The optimized slabs of pure and transition metal (TM)-doped rutile TiO_2 with adsorbed CO and NO are illustrated in Fig. 8. The optimized geometric parameters after the adsorption of CO and NO indicate that the lengths of the Ti–O bonds range from 1.96 to 2.05 angstroms, while the O–Ti–O bond angle varies between 78.39 and 179.47° for both pure and TM-doped TiO_2, suggesting a negligible effect in bond lengths and angles. The results obtained from the geometric optimization show that the Ti–O bond length on the surface of pure rutile TiO_2 without gas is measured at 1.95 Å, which is in close agreement with another computational value of 1.98 Å.[15] The adsorption energy for both pure and TM-doped TiO_2 was computed using eqn (6) ref. 43 and 44 and is presented in Table 2.

$$E_{ads} = E_{material+gas} - E_{material} - E_{gas} \quad (6)$$

Table 2 Calculated adsorption energies (eV) for CO and NO gases on pure rutile TiO_2 as well as on rutile TiO_2 clusters doped with Co, Ni, Cu, and Zn and recovery time τ (s) at 300 K

System	E_{ads} (eV) of CO	E_{ads} (eV) of NO	τ (s) of CO	τ (s) of NO
Pure TiO_2	−0.620	−0.186	2.60×10^{-2}	1.33×10^{-9}
Co-doped TiO_2	−0.898	−0.396	1.22×10^{3}	4.49×10^{-6}
Ni-doped TiO_2	−0.726	−0.639	1.57×10^{0}	5.43×10^{-2}
Cu-doped TiO_2	−0.914	−0.381	2.26×10^{3}	2.51×10^{-6}
Zn-doped TiO_2	−0.949	−0.559	8.76×10^{3}	2.46×10^{-3}

where $E_{material+gas}$, $E_{material}$ and E_{gas} represent the total energy of the gas interacting with the material, the total energy of the doped or pure TiO_2, and the total energy of a gas molecule, respectively.[43,44] The E_{ads} values for all materials when exposed to either CO or NO were observed to be negative, which signifies a spontaneous exothermic reaction, confirming an effective adsorption of the gases on the surfaces of both pure and TM-doped TiO_2.[14,45]

The E_{ads} of CO and NO on pure rutile TiO_2 were determined to be −0.620 eV and −0.186 eV, respectively, demonstrating the material's higher sensitivity to CO in comparison to NO. Moreover, the E_{ads} values confirm that the adsorption of CO occurs *via* a chemisorption mechanism, as the energy values range from −0.5182 to −9.9497 eV.[14,45] In contrast, NO undergoes a physisorption process, with its adsorption energy falling between −0.1036 eV and −0.3109 eV.[14,45] Upon doping, the E_{ads} of gases on TM doped rutile TiO_2 increases, leading to a more stable interaction between the gas and the surface. This stability is beneficial for both the durability and responsiveness of sensors. For CO, the E_{ads} was observed to increase in the following order: Zn–TiO_2 > Cu–TiO_2 > Co–TiO_2 > Ni–TiO_2 > TiO_2 while for NO, the order is Ni–TiO_2 > Zn–TiO_2 > Co–TiO_2 > Cu–TiO_2 > TiO_2. A detailed examination of the E_{ads} values for the gases adsorbed on the TM doped rutile TiO_2 indicates that the adsorption process for both CO and NO transitions to chemisorption following doping, with NO specifically changing from physisorption to chemisorption after the doping process. Additionally, it can be seen that the E_{ads} values of all the materials for CO is much higher than for NO except for Ni-doped TiO_2 where the values were found to be closer confirming that all the pure and TM-doped TiO_2 with the exception of Ni-doped TiO_2 has lower selectivity while the Ni-doped TiO_2 can be used to sense multiple gases confirming its higher selectivity. The dual affinity exhibited by Ni-doped TiO_2 towards CO and NO can be explained by the electronic alterations caused by the incorporation of Ni. The PDOS analysis of the clean surfaces (Fig. 3) indicates that Ni introduces additional states close to the Fermi level and modifies the electronic structure of the neighboring five-fold coordinated Ti (Ti_{5C}) sites through mechanisms of orbital hybridization and charge transfer. This redistribution of electronic density enhances the chemical reactivity of Ti_{5C} sites for the adsorption of both CO and NO. In the case of CO, the increased electron density at Ti_{5C} sites promotes σ donation from the CO 5σ orbital to the surface, as well as π back-donation from surface states into the CO 2π* orbital. Conversely, for NO, this same electronic enhancement facilitates stronger π back-donation into the half-filled NO π* orbital, which accounts for its relatively higher adsorption energy. This general electronic activation mechanism, wherein Ni modifies the characteristics of neighboring Ti_{5C} sites instead of functioning as a direct adsorption center, elucidates the observed dual affinity and differentiates Ni from other dopants that tend to induce more gas-specific effects.

Moreover, comparing the E_{ads} values of CO to NO to both pure and TM-doped materials, it can be concluded that the materials are more sensitive to the reducing CO gas compared to the oxidizing gas NO indicating a better charge transfer with CO. As

calculated in Section 3.4, all the materials were found to be p-type which is expected to have a tendency of electron withdrawing favoring electron transfer from the reducing gas (CO) more favorable and hence higher adsorption energy than the oxidizing gas (NO). This enhanced electron-withdrawing capability is further justified by the p-type nature of the aliovalent TM^{2+} dopants, which creates a more reactive surface for redox-based chemisorption. The electronic states induced by the dopant enhance the binding affinity of gas molecules on the TiO_2 surface. This is evident in the increased adsorption energies relative to the pristine surface, signifying a shift towards chemisorption and suggesting that the dopant sites act as active centers that promote interactions between molecules and the surface.

A similar result was also reported by Amogh A. Sambare *et al.* (2023), who studied CO gas adsorption on transition metal (Co, Cr, Cu, Mn, Mo, and Nb)-doped $BiFeO_3$ using DFT + U + V calculations.[46] Furthermore, doping was confirming from the TDOS and electronic structure in Fig. 3 showed an increased hole conductivity that was confirmed by the down ward shift of the Fermi level towards the VB which consequently can improve the materials electron withdrawing property that led to a stronger chemisorption of even the reducing gas upon doping. Hence, it can be concluded TM-doping can effectively enhance the gas sensing performance of rutile TiO_2 in addition to increasing its selectivity towards reducing and oxidizing gases such as CO and NO.

3.4.2 Recovery time and reusability. The reusability of a gas sensor is determined by how fast it eliminates the adsorbed gas, also called recovery time, and is ready for next use. The recovery time of the pure and TM-doped TiO_2 is calculated using eqn (7) based on the Vant Hoff Arrhenius principle.[47,48]

$$\tau = \nu^{-1} \exp(E_{ads}/k_B T) \quad (7)$$

where ν^{-1} represents the attempt frequency associated with gas adsorption processes, typically ranging from 10^{12} s^{-1} to 10^{13} s^{-1}, taken to be 10^{12} s^{-1}. E_{ads}, k_B and T are the adsorption energy, Boltzmann's constant, and temperature, respectively.

The recovery times for the gases examined, including CO and NO, calculated at room temperature, are presented in Table 2. The results show that pure rutile TiO_2 demonstrates fast recovery times for both CO (26.00 ms) and NO (1.33 ns) at room temperature. This implies weak interactions and remarkable reusability, although it may exhibit limited sensitivity, especially for NO.[51] In contrast, the recovery times for CO when doped with Co, Cu, and Zn in rutile TiO_2 are significantly longer, measuring 1220 s, 2260 s, and 8760 s, respectively. This indicates enhanced adsorption and potentially greater sensitivity, albeit with diminished reusability. The doped systems show a relatively rapid recovery time for NO, with recovery durations of 4.49 μs for Co-doped rutile, 2.51 μs for Cu-doped rutile, and 2.46 ms for Zn-doped rutile. This suggests improved interaction compared to pure rutile TiO_2, while still allowing for a fast reset. The optimal performance is exhibited by Ni-doped rutile TiO_2, which demonstrates moderate recovery times for CO and NO gases, specifically 1.57 seconds and 54.3 milliseconds, respectively. This suggests enhanced gas interaction with commendable recovery times, positioning it as the most suitable choice for practical gas sensing applications where both sensitivity and reusability are essential. In conclusion, the adsorption energy governs the balance between recovery time and reusability.[14] Doped rutile TiO_2 systems are better suited for practical gas sensing applications where stability and long-term efficacy are essential, as they offer enhanced sensitivity and improved reusability, despite necessitating longer recovery periods.

3.5 Gas sensing mechanism

Gas sensing mechanism of the materials under this study work on the principle of electron transfer between the gasses and pure and TM-doped rutile TiO_2 which directly affects its resistivity according to the empirical relation; $R \propto \exp(qV_s/k_B T)$.[49–51] When the TiO_2 sensor is exposed to clean air at its operating temperature, atmospheric oxygen (O_2 (gas)) acts as an electron acceptor. O_2 adsorbs onto the surface and extracts mobile electrons from the semiconductor conduction band, forming negatively charged chemisorbed oxygen ions, such as the O_2^- (ads) ion at low temperatures as follows:

$$O_2\ (g) \rightarrow O_2\ (ads)$$

$$O_2\ (ads) + e^- \rightarrow O_2^-\ (ads)\ (T < 100\ ^\circ C)$$

Once the adsorbed oxygen ion (O_{2ads}^-) is formed by withdrawing electron from the semiconductor, the baseline resistance (R_{air}) increases if the materials is an n-type semiconductor as TiO_2 following the increase in the depletion region. To determine the adsorption mechanism of on the pure TiO_2, looking into the processes by their adsorption energy given in Table 2, the chemisorption process of CO is by reaction of the gas on adsorbed oxygen as follows:[52]

$$2CO\ (gas) + O_2^-\ (ads) \rightarrow 2CO_2\ (gas) + 2e^- \quad (8)$$

This reaction converts the oxygen ion into CO_2 gas and, most critically, releases the previously trapped electron back into the TiO_2 conduction band (see eqn (8)). The potential barrier (eVs) lowers significantly, facilitating the flow of electrons across the grain boundaries. This results an increase conductivity and a corresponding decrease in electrical resistance ($R_{gas} < R_{air}$), for n-type sensors exposed to reducing gases.

In contrast, when NO an oxidizing gas (electron acceptor) is introduced; it weakly adsorbs onto the TiO_2 surface and extracts additional electrons from the conduction band as shown below:

$$NO\ (gas) + e^- \rightarrow NO^-\ (ads)$$

This process the conduction band is forced to bend further upwards, widening the distance between the conduction band edge and the Fermi energy line. The potential barrier (eVs) increases, further restricting electron transport across the semiconductor material. This effect leads to a decrease in conductivity

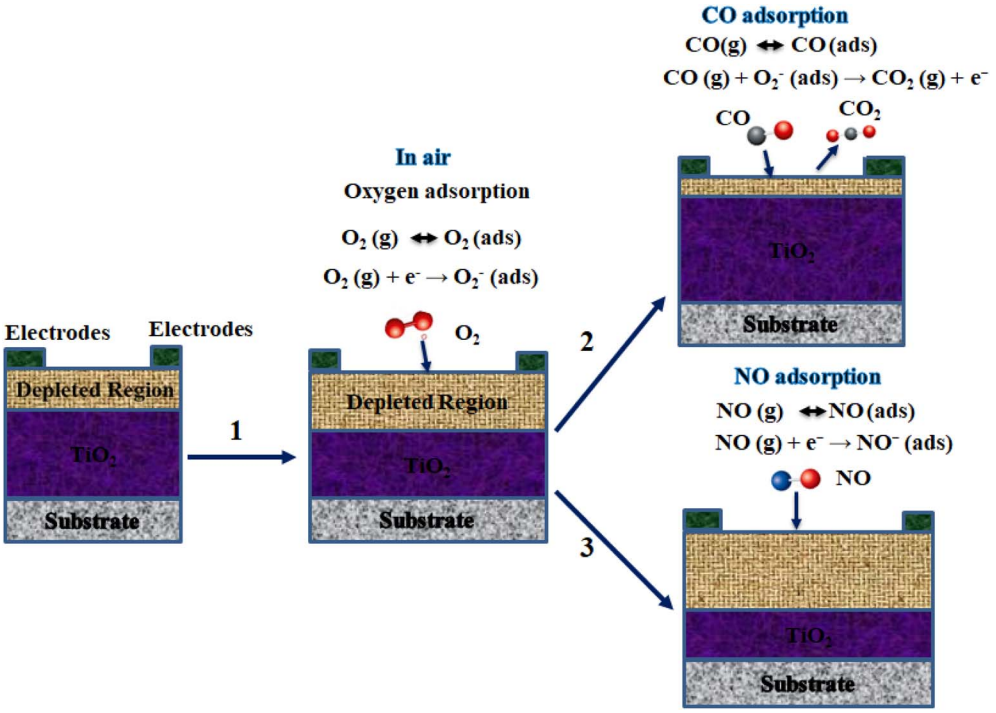

Fig. 9 A schematic representation depicting the gas sensing mechanism of TiO_2 based sensors at room temperature: (1) high resistance in air resulting from the accumulation of surface oxygen ions, (2) reduced resistance during CO adsorption attributed to an increase in electron density, and (3) a significant rise in resistance during NO adsorption due to the strong electron withdrawal by oxidizing gas.

and a measurable increase in electrical resistance ($R_{gas} > R_{air}$) for n-type sensors exposed to oxidizing gases. Upon doping, a similar mechanism to that of pure TiO_2 is anticipated for CO sensing, stronger as confirmed by the higher E_{ads} owing to the increased conductivity. However, the NO sensing mechanism shifts to chemisorption where a definite reaction between the gas. In this context, the TM doping results in the surface functioning as a catalytically active interface, where the dopant centers facilitate electron exchange and redox interactions with the adsorbed gas molecules. In the case of Ni-doped TiO_2, the PDOS analysis reveals that Ni-3d orbitals are capable of donating electrons to CO antibonding orbitals while simultaneously accepting electrons from the lone pairs of NO, thereby elucidating the observed dual affinity and selective adsorption. These interactions mediated by the dopants effectively modulate the surface charge and carrier concentration, thereby enhancing the gas-sensing response. The gas sensing mechanism of CO, NO on pure TiO_2 is summarized in a sketch given in Fig. 9.

4. Conclusion

This research illustrates that the doping of transition metals (Co, Ni, Cu, and Zn) significantly improves the structural, electronic, optical, and gas sensing characteristics of rutile TiO_2, as evidenced by DFT + U calculations pertaining to optoelectronics and gas sensing. Our findings indicate that all dopants cause considerable structural distortion and lattice expansion, which correlates with their atomic radii, thereby triggering a series of advantageous electronic effects. Each doped system displays diminished bandgaps, reaching as low as 2.51 eV for Co, which facilitates visible-light activity and p-type conductivity. The analysis of the projected density of states (PDOS) reveals substantial orbital hybridization and introduces magnetic properties in the Co-, Ni-, and Cu-doped systems. Optical assessments indicate a redshift in absorption, signifying enhanced light harvesting capabilities. The gas sensing performance of doped TiO_2 is markedly improved, with Zn-doped TiO_2 demonstrating the most substantial CO adsorption (−0.949 eV) and Ni-doped TiO_2 showing the highest sensitivity to NO (−0.639 eV). Additionally, the doped systems exhibit superior recovery dynamics and reusability at elevated temperatures. These results position doped rutile TiO_2 as a promising multifunctional material for advanced optoelectronic devices and high-performance gas sensors. Future investigations should focus on exploring the effects of dopant concentration and co-doping strategies to further enhance selectivity and operational stability.

Conflicts of interest

This work is original and has not been published nor is it currently under consideration for publication elsewhere. Moreover, we declared that there is no conflict of interest.

Data availability

The datasets used and/or analyzed during the current study available from the corresponding author on reasonable request.

Supplementary information (SI): figures related to the computational details, structural analysis, and optical properties discussed in the main manuscript. See DOI: https://doi.org/10.1039/d5ra08889e.

Acknowledgements

Prof. Fekadu Gashaw acknowledges the financial support of Addis Ababa University through the Thematic Research Grant (ORA/013/18/25).

References

1 B. Zong, S. Wu, Y. Yang, Q. Li, T. Tao and S. Mao, Smart gas sensors: recent developments and future prospective, *Nano-Micro Lett.*, 2025, **17**, 54.
2 S. Panda, S. Mehlawat, N. Dhariwal, A. Kumar and A. Sanger, Comprehensive review on gas sensors: Unveiling recent developments and addressing challenges, *Mater. Sci. Eng., B*, 2024, **308**, 117616.
3 X. Liu, T. Ma, N. Pinna and J. Zhang, Two-dimensional nanostructured materials for gas sensing, *Adv. Funct. Mater.*, 2017, **27**, 1702168.
4 J. Bai and B. Zhou, Titanium dioxide nanomaterials for sensor applications, *Chem. Rev.*, 2014, **114**, 10131–10176.
5 D. Degler, U. Weimar and N. Barsan, Current understanding of the fundamental mechanisms of doped and loaded semiconducting metal-oxide-based gas sensing materials, *ACS Sens.*, 2019, **4**, 2228–2249.
6 J. Zhao, H. Wang, Y. Cai, J. Zhao, Z. Gao and Y.-Y. Song, The challenges and opportunities for TiO2 nanostructures in gas sensing, *ACS Sens.*, 2024, **9**, 1644–1655.
7 S. M. Al-Jawad, M. Rasheed and Z. Y. Abbas, Effect of doping on the structural, optical and electrical properties of TiO2 thin films for gas sensor, *J. Opt.*, 2024, 1–22.
8 M. Saini, M. Kumar and T. Som, ab initio study of 3d transition metal-doping effects in rutile-TiO2: Role of bandgap tunability in conductivity behaviour, *Appl. Surf. Sci.*, 2017, **418**, 302–307.
9 I. Østrøm, M. A. Hossain, P. A. Burr, J. N. Hart and B. Hoex, Designing 3d metal oxides: selecting optimal density functionals for strongly correlated materials, *Phys. Chem. Chem. Phys.*, 2022, **24**, 14119–14139.
10 A. Bajaj and H. J. Kulik, Molecular DFT+ U: a transferable, low-cost approach to eliminate delocalization error, *J. Phys. Chem. Lett.*, 2021, **12**, 3633–3640.
11 S. A. Tolba, K. M. Gameel, B. A. Ali, H. A. Almossalami, and N. K. Allam, The DFT+ U: Approaches, accuracy, and applications, in *Density Functional Calculations-Recent Progresses of Theory and Application*, IntechOpen, 2018.
12 M. Samat, A. Ali, M. Taib, O. Hassan and M. Yahya, Hubbard U calculations on optical properties of 3d transition metal oxide TiO2, *Results Phys.*, 2016, **6**, 891–896.
13 Z. Yan, Y. Zhang, W. Kang, N. Deng, Y. Pan, W. Sun, J. Ni and X. Kang, TiO2 gas sensors combining experimental and DFT calculations: a review, *Nanomaterials*, 2022, **12**, 3611.
14 O. H. Abd-Elkader, M. A. Sakr, M. A. Saad, H. Abdelsalam and Q. Zhang, Electronic and gas sensing properties of ultrathin TiO2 quantum dots: A first-principles study, *Results Phys.*, 2023, **52**, 106804.
15 F. T. Geldasa and F. B. Dejene, Exploration of vanadium and rhenium co-doped TiO2 for enhanced photocatalytic performance via first principle density functional theory investigation, *Phys. Scr.*, 2025, **100**, 085924.
16 F. T. Geldasa and F. B. Dejene, Effects of S Doping and Oxygen Vacancy on the Physical Properties of Rutile TiO2 for Photocatalysis Applications Based on Density Functional Theory Study, *Materials*, 2025, **18**, 1688.
17 S. M. Rasul, D. R. Saber and S. B. Aziz, Role of Titanium replacement with Pd atom on band gap reduction in the anatase Titanium Dioxide: First-Principles calculation approach, *Results Phys.*, 2022, **38**, 105688.
18 F. T. Geldasa, M. A. Kebede, F. G. Hone and E. T. Jira, Influence of non-metals doping on the structural, electronic, optical, and photocatalytic properties of rutile TiO2 based on density functional theory computations, *Comput. Condens. Matter*, 2024, **41**, e00970.
19 F. T. Geldasa, F. B. Dejene, M. A. Kebede, F. G. Hone and E. T. Jira, Density functional theory study of Chlorine, Fluorine, Nitrogen, and Sulfur doped rutile TiO2 for photocatalytic application, *Sci. Rep.*, 2025, **15**, 3390.
20 M. Capdevila-Cortada, Z. Łodziana, and N. López, in *Performance of DFT + U Approaches in the Study of Catalytic Materials*, ACS Publications, 2016, pp. 8370–8379.
21 S. K. Iyemperumal and N. A. Deskins, Activation of CO 2 by supported Cu clusters, *Phys. Chem. Chem. Phys.*, 2017, **19**, 28788–28807.
22 M. M. Hasan, A. Kabir and M. Kamruzzaman, The structural, elastic, electronic, magnetic and optical properties of SrNiO3 perovskite: A DFT and DFT+ U study, *Results Phys.*, 2022, **41**, 105920.
23 V. Christhunathan, P. Farràs and M. Tong, First-principles study of electronic properties of Zn and La doped and co-doped anatase TiO2, *AIP Adv.*, 2023, **13**, 125013.
24 K. Ohno, R. Sahara, T. Nanri and Y. Kawazoe, Optical properties of rutile TiO2 with Zr, Mo, Zn, Cd impurities, *Comput. Condens. Matter*, 2024, **41**, e00977.
25 N. Gonzalez Szwacki, P. Fabrykiewicz, I. Sosnowska, F. o. Fauth, E. Suard and R. Przeniosło, Orthorhombic symmetry and anisotropic properties of rutile TiO2, *J. Phys. Chem. C*, 2023, **127**, 19240–19249.
26 H. Chen, X. Li, R. Wan, S. Kao-Walter, Y. Lei and C. Leng, A DFT study on modification mechanism of (N, S) interstitial co-doped rutile TiO2, *Chem. Phys. Lett.*, 2018, **695**, 8–18.
27 P. Santos-Aguilar, J. Bernal-Ramírez, E. Vazquez-Garza, L. Y. Vélez-Escamilla, O. Lozano, G. d. J. Garcia-Rivas and F. F. Contreras-Torres, Synthesis and characterization of rutile TiO2 nanoparticles for the toxicological effect on the H9c2 cell line from rats, *ACS Omega*, 2023, **8**, 19024–19036.
28 S. Sahoo, G. Ghorai, K. Ghosh, B. Das, M. K. Sikdar and P. K. Sahoo, Anharmonicity of optical phonon modes in copper doped rutile TiO2 nanorod composed microflowers, *AIP Adv.*, 2021, **11**, 105013.
29 H. Heffner, R. Faccio and I. López-Corral, C–doped TiO2 (B): a density functional theory characterization, *Appl. Surf. Sci.*, 2021, **551**, 149479.
30 F. Amano, A. Yamamoto and J. Kumagai, Highly Active Rutile TiO2 for Photocatalysis under Violet Light Irradiation at 405 Nm, *Catalysts*, 2022, **12**(10), 1079.

31 W. C. P. Wanniarachchi, T. Arunasalam, P. Ravirajan, D. Velauthapillai and P. Vajeeston, Hybrid functional study on electronic and optical properties of the dopants in anatase TiO2, *ACS Omega*, 2023, **8**, 42275–42289.

32 Z. Zhang, Q. Hou, M. Qi and S. Sha, First principles of Fe/Co/Ni doping and the coexistence of O vacancy in the magnetic and optical properties of rutile TiO2 (110) surface, *Phys. Scr.*, 2022, **97**, 045815.

33 A. Iwaszuk and M. Nolan, Charge compensation in trivalent cation doped bulk rutileTiO2, *J. Phys.: Condens. Matter*, 2011, **23**, 334207.

34 Y. Matsumoto, M. Katayama, T. Abe, T. Ohsawa, I. Ohkubo, H. Kumigashira, M. Oshima and H. Koinuma, Chemical trend of Fermi-level shift in transition metal-doped TiO2 films, *J. Ceram. Soc. Jpn.*, 2010, **118**, 993–996.

35 F. T. Geldasa, M. A. Kebede, M. W. Shura and F. G. Hone, Different metal dopants effects on the structural, electronic, and optical properties of β-PbO: a density functional theory study, *Eur. Phys. J. Plus*, 2023, **138**, 165.

36 F. T. Geldasa, The structural, electronic, and optical properties of metals doped litharge PbO: A density functional theory study, *Eur. Phys. J. B*, 2024, **97**, 78.

37 C. Tesvara, C. Walenta and P. Sautet, Oxidative decomposition of dimethyl methylphosphonate on rutile TiO 2 (110): the role of oxygen vacancies, *Phys. Chem. Chem. Phys.*, 2022, **24**, 23402–23419.

38 H. Perron, C. Domain, J. Roques, R. Drot, E. Simoni and H. Catalette, Optimisation of accurate rutile TiO2 (110),(100),(101) and (001) surface models from periodic DFT calculations, *Theor. Chem. Acc.*, 2007, **117**, 565–574.

39 T. Zheng, C. Wu, M. Chen, Y. Zhang and P. T. Cummings, A DFT study of water adsorption on rutile TiO2 (110) surface: The effects of surface steps, *J. Chem. Phys.*, 2016, **145**, 044702.

40 R. Panta and V. Ruangpornvisuti, Unusual adsorption behavior of hydrogen molecules on Zr–doped perfect and oxygen–vacancy defective rutile TiO2 (110) surfaces: Periodic DFT study, *Int. J. Hydrogen Energy*, 2019, **44**, 32101–32111.

41 T. T. Thoa, T. T. Nguyen, H. Van Hung and N. T. M. Hue, Slab models of rutile TiO2 (110) surface: DFT and DFT+ U calculations, *Vietnam J. Chem.*, 2023, **61**, 563–570.

42 J. P. P. Ramalho, F. Illas and J. R. Gomes, Adsorption of CO on the rutile TiO 2 (110) surface: a dispersion-corrected density functional theory study, *Phys. Chem. Chem. Phys.*, 2017, **19**, 2487–2494.

43 M. I. Khan, M. Hassan, A. Majid, M. Shakil and M. Rafique, DFT perspective of gas sensing properties of Fe-decorated monolayer antimonene, *Appl. Surf. Sci.*, 2023, **616**, 156520.

44 Y. Yu and C. Dai, DFT study of gas adsorption and sensing based on noble metal (Ag, Au and Pt) functionalized boron selenide nanosheets, *Phys. E*, 2021, **125**, 114409.

45 Y. Qu, L. Qin, M. Guo, X. Liu and Y. Yang, Multilayered molecularly imprinted composite membrane based on porous carbon nanospheres/pDA cooperative structure for selective adsorption and separation of phenol, *Sep. Purif. Technol.*, 2022, **280**, 119915.

46 A. A. Sambare, R. Pawar and M. Shirsat, A DFT investigation on transition metal (Co, Cr, Cu, Mn, Mo and Nb)-doped bismuth ferrite oxide (BiFeO3) for CO gas adsorption, *Theor. Chem. Acc.*, 2023, **142**, 61.

47 M. I. Khan, M. I. Akber, M. Gul, T. Iqbal, S. S. Alarfaji and A. Mahmood, Exploring the sensing potential of Fe-decorated h-BN toward harmful gases: a DFT study, *RSC Adv.*, 2024, **14**, 7040–7051.

48 V. Parey, B. M. Abraham, N. K. Gaur and R. Thapa, First-principles study of two-dimensional B-doped carbon nanostructures for toxic phosgene gas detection, *ACS Appl. Nano Mater.*, 2022, **5**, 12737–12745.

49 H. Ji, W. Zeng and Y. Li, Gas sensing mechanisms of metal oxide semiconductors: a focus review, *Nanoscale*, 2019, **11**, 22664–22684.

50 K. L. Morulane, Z. P. Tshabalala, H. C. Swart and D. E. Motaung, Assembly of np In2O3-Co3O4 heterostructures and their surface and structural analyses towards trace level detection of acetone, *Appl. Surf. Sci.*, 2024, **671**, 160714.

51 K. L. Morulane, H. C. Swart and D. E. Motaung, A review on topical advancement and challenges of indium oxide based gas sensors: Future outlooks, *J. Environ. Chem. Eng.*, 2024, **12**, 112144.

52 A. Pathania, N. Dhanda, R. Verma, A.-C. A. Sun, P. Thakur and A. Thakur, Metal oxide chemoresistive gas sensing mechanism, parameters, and applications, *ECS Sens. Plus*, 2024, **3**, 013401.